Ultrafast multiphoton pump-probe photoemission excitation pathways in rutile TiO_{2}(110)

Adam Argondizzo, Xuefeng Cui, Cong Wang, Huijuan Sun, Honghui Shang, Jin Zhao, and Hrvoje Petek

Phys. Rev. B **91**, 155429 — Published 27 April 2015

DOI: 10.1103/PhysRevB.91.155429

Ultrafast multiphoton pump-probe photoemission excitation pathways in rutile $TiO_2(110)$

Adam Argondizzo[1], Xuefeng Cui[1,2], Cong Wang[1], Huijuan Sun[2,3], Honghui Shang[4], Jin Zhao[1,2,3], and Hrvoje Petek[1]
[1]*Department of Physics and Astronomy, University of Pittsburgh, Pittsburgh, Pennsylvania 15260, USA*
[2]*Department of Physics and ICQD/Hefei National Laboratory for Physical Sciences at Microscale, University of Science and Technology of China, Hefei, Anhui 230026, China*
[3]*Synergetic Innovation Center of Quantum Information & Quantum Physics, University of Science and Technology of China, Hefei, Anhui 230026, China*
[4]*Fritz-Haber-Institut der Max-Planck-Gesellschaft, Faradayweg 4-6, 14195 Berlin, Germany*

Abstract

We investigate the spectroscopy and photoinduced electron dynamics within the conduction band of reduced rutile $TiO_2(110)$ surface by multiphoton photoemission (*m*PP) spectroscopy with wavelength tunable ultrafast (~20 fs) laser pulse excitation. Tuning the *m*PP photon excitation energy between 2.9 and 4.6 eV reveals a nearly degenerate pair of new unoccupied states located at 2.73±0.05 and 2.85±0.05 eV above the Fermi level, which can be analyzed through the polarization and sample azimuthal orientation dependence of the *m*PP spectra. Based on the calculated electronic structure and optical transition moments, as well as related spectroscopic evidence, we assign these resonances to transitions between Ti 3*d*-bands of nominally t_{2g} and e_g symmetry, which are split by crystal-field. The initial states for the optical transition are the reduced Ti^{3+} states of t_{2g} symmetry populated by formation oxygen vacancy defects, which exist within the band gap of TiO_2. Furthermore, we studied the electron dynamics within the conduction band of TiO_2 by three-dimensional (3D) time-resolved pump-probe interferometric *m*PP measurements. The spectroscopic and time-resolved studies reveal competition between *2*PP and *3*PP processes where the t_{2g} - e_g transitions in the *2*PP process saturate, and are overtaken by the *3*PP process initiated by the band gap excitation from the valence band of TiO_2.

I. Introduction

The physics and chemistry of TiO_2 have been of interest due to its notable photocatalytic and photovoltaic properties.[1, 2] The ability of TiO_2 colloids to decompose chemicals interacting with their surfaces upon band gap excitation has been demonstrated and utilized in many applications including clean solar energy conversion by the splitting of water into H_2 and O_2, self-cleaning windows, environmental remediation, and others.[3-7] Moreover, photoexcited electron and hole dynamics play a decisive role for the efficiency of TiO_2 colloid based dye-sensitized photoelectrochemical solar cells.[2, 8]

The photocatalytic and photovoltaic activity of a semiconductor depends on the carrier excitation and relaxation processes in the near-surface region.[9, 10] The photoexcited electron dynamics in TiO_2, primarily for colloidal rutile and anatase polymorph samples, have been studied by optical methods over a broad frequency range from the THz to ultraviolet (UV).[11-21] In optical experiments UV light excites carriers across the band gap and various color probe light absorption or emission processes report on the ultrafast carrier energy and momentum evolution. It is difficult, however, to assign features in optical spectra to the specific carrier type and its chemical potential, within a temporally and spatially evolving carrier distribution. Such information is essential for establishing the potential of photoexcited carriers to catalyze chemical reactions, or to drive current within photoelectrochemical cells.

Time-resolved multi-photon photoemission (TR-*m*PP) spectroscopy, which is illustrated by the energy diagram in Fig. 1, has significant advantage in being able to probe the time-dependent electron populations at specific energy and momentum in the near-surface region of a solid.[22, 23] TR-*2*PP has been applied to the spectroscopy and dynamics of single crystal rutile $TiO_2(110)$ surfaces under ultrahigh vacuum (UHV) conditions in the contexts of both photocatalysis and dye sensitized solar cells.[24-33] The well known surface preparation, properties, and chemistry make rutile $TiO_2(110)$ well suited for studies of elementary surface and bulk charge carrier processes triggered by photoexcitation in metal oxides.[4, 6, 7]

Previous TR-*2*PP experiments on clean and protic solvent covered $TiO_2(110)$ surfaces with 400 nm (3.1 eV) excitation focused on the surface electronic structure.[24-29] For the clean $TiO_2(110)$ surface the work function was found to depend strongly on surface preparation methods. Under reducing conditions the work function decreased through generation of near-surface O atom vacancy defects.[24] Upon annealing in the oxidizing O_2 atmosphere to produce a nearly stoichiometric surface, the work function increased up to 5.6 eV. With 3.1 eV light, *2*PP can probe only the Ti-3*d* defect states below the conduction band minimum (CBM; Fig. 1).[34] The *2*PP intensity of this defect band depends on the concentration of the surface and bulk O-atom vacancy defects, because desorption of O_2 molecules leaves a charge of $2e^-$ per O atom vacancy. Photoemission spectra record this defect band as a broad peak with the maximum density 0.8 eV below the Fermi level (E_F).[6, 35]

Interferometric pump-probe TR-*2*PP measurements with ~1 nJ, 10 fs, 3.1 eV laser pulses were used to probe the electron dynamics upon excitation of the Ti-3*d* defect band [25]. These measurements could not resolve the hot electron lifetimes in the 1.5-3.1 eV energy range above E_F either because the lifetimes were too short, or the intermediate states in the *2*PP process were virtual. The latter possibility was consistent with an apparent lack of distinct spectroscopic features in the *2*PP spectra due to unoccupied intermediate surface or bulk states of TiO_2.[24, 25] The experimental results were also consistent with theoretical calculations of fast hot electron relaxation in TiO_2 by electron-phonon (e-p) and electron-electron (e-e) scattering.[36, 37] Because of the fixed excitation wavelength, TR-*2*PP measurements on TiO_2 could not address the properties of the photocatalytically relevant CBM carriers as has been done for ZnO.[38, 39]

*2*PP studies have also been performed on molecule covered TiO_2 surfaces. The adsorption of protic solvents, such as H_2O and CH_3OH, introduced a new surface state at 2.3-2.4 eV above E_F, which has been dubbed the "wet electron" state.[25, 27-29] According to DFT and many-body perturbation theory calculations, these surface states correspond to diffuse orbitals bound to several non-hydrogen-bonded H atom centers.[40-43] The wet electron states are excited directly by photoinduced charge transfer from the Ti-3*d* defect band.[25, 27, 44] Their lifetimes were found to vary form <10 fs at low H_2O coverage to picosecond timescales at multilayer coverage of CH_3OH, where the "wet" orbitals are decoupled from the TiO_2 substrate.[25, 27]

Other TR-*2*PP measurements by Matsumoto, and Willig addressed the charge injection from chemisorbed dye molecules into the CB single crystal rutile TiO_2(110) surfaces.[30-33] The charge injection rates were found to depend on the functional group anchoring the dye molecules to the TiO_2 surface. In the case of the TR-*2*PP measurements on catechol covered TiO_2 surface, the timescale for the primary injection into the semiconductor was judged to be instantaneous, whereas the subsequent population decay occurred in a biexponential manner with ~100 fs and ~1 ps components, without significant energy relaxation.[31] The decay was thus attributed to charge transport from the TiO_2 surface into the bulk. Such long hot electron lifetimes were difficult to reconcile with the substantially faster dynamics at comparable energies on clean and protic molecule covered surfaces.[25, 27, 45] as well as the more recent measurements of hot electron relaxation in the CB of ZnO.[38, 39]

Here we report on spectroscopy and femtosecond timescale photoexcitation dynamics within the conduction band (CB) of TiO_2 by TR-*m*PP spectroscopy using tunable UV femtosecond laser excitation to excite the *2*PP and *3*PP processes. A thorough understanding of the surface and bulk excitation and relaxation pathways is necessary for the interpretation of *m*PP spectra and electron dynamics of molecule-covered TiO_2 surfaces. Using a wavelength tunable femtosecond laser excitation source, we extend the spectroscopy and dynamics at rutile TiO_2(110) surface to a broad energy range below and above band gap excitation. Excitation wavelength, polarization, and crystal azimuthal orientation dependent measurements reveal a pair of nearly degenerate unoccupied states located at 2.73±0.05 and 2.85±0.05 eV above the E_F, which resonantly enhance the *2*PP process at 3.66 eV from the occupied Ti-3*d* defect states. Based on the calculated electronic structure of rutile TiO_2 and other spectroscopic evidence, we assign this resonance to the e_g component of the crystal field-split Ti-3*d* conduction band. TR-*2*PP measurements reveal unusual photoexcitation dynamics associated with saturation of the *2*PP process *via* the resonant t_{2g}-e_g transition, which occurs simultaneously and in competition with the *3*PP process from the valance band maximum (VBM). The dynamics of such intra *d*-band excitations are of significant interest for their potential impact on photocatalysis and because in correlated metal oxide materials they can optically trigger electronic and structural phase transitions.[46-48] The new information expands our understanding of the spectroscopy and electron dynamics of TiO_2 and related metal oxides under high excitation density, nonlinear conditions.

II. Experimental Details

To overcome the limitations of previous TR-*2*PP experiments, which employed 400 nm light pulses from the second harmonic of a Ti:sapphire laser oscillator, we developed a new TR-*m*PP system based on excitation with a dual non-collinear optical parametric amplifier (NOPA) source.[49, 50] The NOPA is pumped by the second and third harmonics of a CMXR Impulse Yb-doped fiber laser operating at 1,035 nm with a variable repetition rate from 0.2 to 2 MHz, 10 µJ per pulse energy, and ~250 fs pulse duration. The white light continuum generated by the fundamental beam seeds the amplification of the parametric emission, which is pumped by the second and third harmonics, to generate tunable pulses in the 680-900 and 500-650 nm (1.4-1.8 and 1.9-2.5 eV) bands with typically <15 fs pulse duration. After amplification the NOPA outputs are collimated and compressed by multiple passes between matched pairs of negative dispersion mirrors with second and third-order dispersion compensation. Frequency doubling of the NOPA output in BBO crystals produces tunable excitation pulses in the 270-420 nm (2.9-4.6 eV) band with ~20 fs duration. The experiments are performed with single color excitation at a pulse repetition rate of 1.25 MHz. The $TiO_2(110)$ single crystal is aligned with its [001] axis in the optical plane, unless specified otherwise. The laser polarization with respect to the optical plane is adjusted with a $\lambda/2$ plate.

The $TiO_2(110)$ single crystal samples from Princeton Scientific Corp. are prepared by multiple sputter and annealing cycles at a background pressure of $<5*10^{-10}$ mbar. The final annealing occurs in an oxygen environment of $1*10^{-8}$ mbar to reduce the concentration of surface oxygen vacancies. The sample quality is judged from the work function edge, which is typically in the 5.2-5.5 eV range, and sharp low energy electron diffraction (LEED) peaks. Surface defects or chemisorbed impurities, such as H_2O lower the work function from that of a clean surface, as established previously.[24]

*m*PP spectra are recorded with a SPECS Phoibos 100 hemispherical analyzer, which is equipped with a Delay Line Detector (DLD). The DLD records two-dimensional energy *vs*. momentum photoelectron distributions in an electron counting mode. A 1V bias is applied between the sample and the analyzer. The UHV chamber pressure is maintained at $<2*10^{-10}$ mbar during the experiments. Under these conditions the work function typically decreases from 5.4 to 5.0 eV within approximately 6 hours due to reaction with residual gases in the chamber. Experiments are carried out at 600, 293 and ~100 K. The *m*PP spectra reported herein are all taken at 293 K to minimize adsorption of background gases on the surface.

In addition, we perform interferometric time-resolved two-pulse correlation (ITR-*2*PC) measurements of *m*PP using a Mach–Zehnder interferometer to generate two identical pulse replicas with a delay scan range of ~300 fs and <50 as scan increment.[22, 51] The interferometer optics limit the ITR-*2*PC measurements to the 340-450 nm wavelength range. The pump-probe scans provide three-dimensional (3D) data consisting of time-dependent *m*PP spectra, *i.e.*, the photoelectron counts vs. energy, momentum, and pump-probe delay time.[52]

The laser pulse duration is characterized *in situ* by ITR-2PC measurements on polycrystalline molybdenum sample holder, which has an inhomogenously broadened spectrum and fast (<10 fs) hot electron lifetimes. The analysis of the autocorrelation measurements gives typical UV pulse durations of ~20 fs. The pulse duration increases with the photon energy due to the dispersion in the optical path and limitations of the negative dispersion mirrors for compensation of dispersion in the UV region.

In addition to the *2*PP spectra of the clean $TiO_2(110)$ surface, we deposit methanol to establish the bulk origin of the newly discovered spectroscopic features. Methanol vapor is introduced into the UHV chamber using a doser at a background pressure of $5*10^{-9}$ mbar until 1 ML coverage is achieved. The coverage is determined from the work function decrease.[26]

III. Results and Discussion

Previous *2*PP studies of $TiO_2(110)$ surface with 3.1 eV excitation showed broad, featureless spectra, with photoelectron count rate and work function onset that depended on the surface preparation protocols.[24] Reducing the surface populated the Ti-3*d* defect states. Consequently, the *2*PP spectra had low work functions and high count rates from the Ti-3*d* defect states. By contrast, nearly stoichiometric surfaces had high work functions and small count rates.[24]

The high pulse energy and tunability of the NOPA system, compared with the previously used Ti:sapphire laser, allow us to probe the TiO_2(110) surface with higher sensitivity and greater discrimination of the optical excitation pathways. The energy diagram in Fig. 1 shows the possible excitation pathways available for the range of photon energies used in our experiments as well as the electron relaxation pathways. As in the previous experiments, the primary excitation is from the Ti-3*d* defect band.[24] The Fermi level of reduced TiO_2 is typically reported to be 0.1-0.3 eV below the CBM.[53] Because we cannot determine this quantity, in the following discussion we assume a value of 0.2 eV for the CBM-E_F energy difference. The indirect optical band gap of TiO_2 rutile of 3.0 eV[54] is within the employed photoexcitation energy range, but the band gap excitation does not contribute to the *2*PP signal unless the two-photon energy is sufficient to excite electrons from the VBM to above the vacuum level, E_{vac}, as already explained. The band gap excitation can contribute to a *3*PP process, however, if the first photon excites across the band gap and subsequent two photons excite CB electrons to above the E_{vac}. Rutile TiO_2 becomes strongly absorbing at the onset of the direct band gap at 3.6 eV, with the absorption maximum occurring at 4.0 eV[54, 55]

1. 2PP and 3PP spectra

The *2*PP spectra of a clean TiO_2(110) surface excited with *p*-polarized light in the 315-385 nm (3.22-3.95 eV) range are shown in Fig. 2(a). With 3.22 eV NOPA excitation, the *2*PP spectra resemble the previously reported ones with 3.10 eV excitation by the second harmonic of a Ti:sapphire oscillator[24, 25] Tuning the excitation to higher photon energies, however, reveals a new feature. As the photon energy is increased from 3.22 eV, there is rising *2*PP intensity at the E_F edge (the high energy edge of the spectra), which emerges into a clear resonance for 3.66 eV excitation. An angle resolved spectrum measured with 3.66 eV excitation in Fig. 3 shows weak band dispersion corresponding to an effective mass of $>3m_e$ (m_e is the free electron mass). This is the lower bound on the electron mass because of the weak dispersion and broad resonance width.

To gain further information on the newly found resonance, we also measure *2*PP spectra for a series of photon energies with both *s*- and *p*-polarized light and the TiO_2 crystal oriented either with its [001] or $[1\bar{1}0]$ crystalline axis in the optical plane. The *2*PP spectra depend on the crystal orientation because of the anisotropy of the rutile crystal, and consequently its band structure.[54]

Typical *2*PP spectra of the anisotropic response with 3.26 eV excitation are shown in Fig. 2(b). The resonance peak appears in *2*PP spectra excited with both polarizations and crystal orientations, but with distinct lineshapes and slight energy shift. The background emission near the work function edge is much weaker for *s*-polarization, as observed previously.[25]

As expected, the anisotropy of the rutile TiO_2 results in strong dependence of *2*PP spectra on the azimuthal orientation of the sample and the light polarization with respect to the optical plane. The resonance can have either a sharp and intense, or a broad and weak character depending on the direction of the excitation field $\vec{E}$ with respect to the crystalline axis. Moreover, the resonance shifts from 2.85 to 2.73 eV between the two characteristic spectra. The sharp/intense character is observed when a component of $\vec{E}$ points in the $[\bar{1}10]$ direction, whereas the broad/weak character occurs when a component of $\vec{E}$ points along the [001] direction. We will propose the assignment in this section and report on the particulars of the anisotropic response of TiO_2 in a future publication.

Measurements of *2*PP intensity maximum *vs*. the excitation photon energy for *p*-polarized $\vec{E}$ and the crystal oriented with the [001] axis in the optical plane (Fig. 4) reveal the new resonance to be due to an unoccupied state 2.8 eV above E_F, which serves as a resonant intermediate in the *2*PP process from the occupied Ti-3*d* defect states. The Fig. 2(a) inset shows the intensity of the observed peak relative to the intensity of the work function edge for the various excitation wavelengths. The *2*PP intensity maximum of the resonance peak occurs for 3.66 eV excitation. This analysis locates the maximum of the initial defect state density at 0.85 eV below E_F [inset of Fig. 2(a)], which is consistent with the defect state density maximum found in conventional photoemission spectra.[6, 35] The magnitude of the resonance enhancement for excitation from the defect states depends on the defect density, but its energy distribution remains constant.

Because the 2.8 eV state has not been reported in the previous optical or *2*PP experiments on TiO_2, we consider its assignment. The only resonances observed in *2*PP measurements on TiO_2 have been with the extrinsic wet electron states on H_2O and CH_3OH covered TiO_2(110) surfaces.[25, 26, 28, 40] Although at 1 ML coverage of H_2O or CH_3OH the wet electron states are at 2.3-2.4 eV above E_F, at lower coverages they have been reported to shift to higher energy, because fewer solvating OH or CH bonds are available for its stabilization.[25] The assignment to the wet electron states to molecular chemisorption from the residual gas in UHV chamber can be excluded, however, because that requires time, whereas the 2.8 eV resonance exists immediately after the sample annealing at 600 K. Surface OH formed by dissociation of H_2O can be excluded as a potential carrier of the spectrum, because it desorbs at 520 K, whereas the resonance is present in *2*PP spectra at 600 K just as at 293 and 100 K.[56]

We further test origin of the 2.8 eV resonance by depositing a monolayer of methanol onto the TIO_2 surface, and measuring *2*PP spectra before, during, and after the deposition. Such spectra (not shown) show that the wet electron and the 2.8 eV states are spectroscopically *distinct*, with the former being adsorbate induced, and the latter intrinsic to TiO_2. Moreover, a methanol monolayer does not quench the 2.8 eV resonance, which determines its origin in the bulk of TiO_2. Therefore, we search for an assignment in the electronic band structure of TiO_2. In the following discussion we assume that the trapped electrons below the CBM have the same orbital symmetry as the bulk electronic bands of TiO_2 near the CBM.[57]

Because the CB of TiO_2 is derived from the Ti-3*d* states, the most obvious assignment of the 2.8 eV resonance is to t_{2g}-e_g transitions between the crystal field-split 3*d*-conduction bands. To see that this is reasonable, one does not need to look any further than a Ti:sapphire laser, which derives its lasing properties from the t_{2g}-e_g absorption (and consequently stimulated emission) of Ti^{3+} ions within the crystal field of Al_2O_3; the absorption peak for this transition is at 500 nm (2.48 eV).[58]

The assignment of the 2.8 eV resonance to t_{2g}-e_g transitions is fully supported by the recent many-body perturbation theory calculations of TiO_2 band structure.[42, 54, 59] To confirm, we calculate the t_{2g}-e_g optical transition density within the density functional theory (DFT). The calculation at this level of theory is sufficient because errors in calculating the quasiparticle band gap within DFT cancel when considering transitions between the unoccupied states.[54, 60]

The calculations are performed using SIESTA code[61] using the generalized gradient approximation for the exchange-correlation density functional (PBE).[62] With a double-zeta polarized (DZP) numerical basis set a good agreement is reached with results obtained with a plane wave basis. The geometries are fully relaxed until the force on each atom is less than 0.04eV/ Å. The lattice constants used are a= 4.59 and c=2.95 Å. The rutile TiO_2 bulk is calculated using (1×1) unit cell and a Monkhorst-Pack grid of $(6\times6\times9)$ k points. The transition dipole moment is defined as:

$$T^{i}_{n',n}(k) = \left\langle \psi_{n'k} \middle| \nabla_i \middle| \psi_{nk} \right\rangle \tag{1}$$

and the transition density is calculated from $T^{i*}_{n',n}(k)T^{i}_{n',n}(k)$ at the Γ point. To obtain the transition density, we occupy the CB with one excess electron. Furthermore, we consider transitions from both the CBM and CBM+1 bands, which are separated by only 0.12 eV at the Γ point and have predominantly $d_{xy}+d_{xz}$ and d_{xy} orbital character. Figure 5 and the Supplemental Fig. S1[63] show the calculated spatial distributions of orbitals involved in the optical transitions at ~3 eV from the CBM, the band structure of rutile TiO_2, and the calculated transition densities. The calculations predict that two transitions to e_g bands with the d_{z^2} and $d_{xz}+d_{yz}$ orbital character at 2.87 and 3.12 eV can contribute to the *2*PP spectra.

The measured azimuthal orientation and polarization dependent *2*PP spectra in Fig. 2b are consistent with the calculated transition densities in Fig. 5c in that $\vec{E}$ pointing in the $[\bar{1}10]$ direction corresponds to the highest transition density and shift of the resonance to higher energy, as compared to when $\vec{E}$ points in the [001] direction. If the initial state has the symmetry of CBM, when $\vec{E}$ points in the $[\bar{1}10]$ direction the transition density is much smaller than when it points in the [001] direction, in contradiction with the experiment [Supplemental Fig. S1].[63] Although the observed behavior is consistent with transitions from defects states of the CBM+1 symmetry, it does no exclude some contribution from the CBM.

The assignment to the t_{2g}-e_g transition is further corroborated by other experimental evidence. Weak optical *d-d* transitions have also been reported at 2.30 and 2.92 eV in reduced rutile samples.[64] In X-ray absorption (XAS), X-ray photoemission (XPS), inverse photoemission (IPS), and electron-energy loss spectroscopy (EELS) measurements features corresponding to the t_{2g}-e_g band splitting in a range of 2.1-3.0 eV have been reported.[65-68] Thus, our measured peak at 2.8 eV above E_F and its assignment to the e_g band are fully consistent with the DFT calculations and other spectra.

The optical transitions between the t_{2g} and e_g bands may be important for optical spectra of photoexcited TiO_2. If the CB is populated by band gap excitation of TiO_2, the photoexcited carriers could be detected *via* the t_{2g}-e_g transition in transient absorption experiments. Absorption features in the blue-green region of the optical spectrum have been assigned to trapped holes[17, 64] Our results, however, clearly show that the CB electrons also absorb in the same energy region. Therefore, the t_{2g}-e_g transition may be beneficial for studying the CBM dynamics of photoexcited carriers, especially by *m*PP spectroscopy where the electron and hole levels are unambiguously distinguished.

The t_{2g}-e_g transition exhibits additional features, which illuminate the photoexcitation dynamics in TiO_2. The most notable feature is the variation of the *m*PP spectral width of the e_g peak with increasing photon energy, which can be seen in Fig. 2(a). We attribute this characteristic to a combination of effects, including: *i*) the variation in pulse duration of the laser depending on wavelength; *ii*) the broad distribution of defect states, which have a sharp cut off at E_F; and *iii*) the increasing contribution of *3*PP component in the predominantly *2*PP spectra, which sets in as the photon energy is tuned into the direct band gap of TiO_2. This last aspect will be discussed next.

In addition to the peak broadening, the *m*PP spectra exhibit an apparent shift of the e_g peak to a higher energy as the laser intensity is increased (Fig. 6). This is not an artifact of space charge distortion of the photoelectron distribution, because the photoelectron yield from TiO_2 is much less than for metal surfaces under conditions where the distortions are not observed, and more directly, because the work function edge *does not* experience a shift. We will show that the shift occurs because the defect state density is low, and can be depleted at high laser fluences, leading to saturation of the transition. The low density of defect states makes it easier to saturate the transition relative to bulk interband transitions. Simultaneously, the band gap excitation of TiO_2 can populate the CB, so that that the *3*PP photoelectron yield from the valence band (VB; see Fig. 1) can overcome that of *2*PP from the defect states. The *3*PP excitation can occur *via* a coherent three-photon absorption, or *via* a sequential process where electrons excited to CB relax before absorbing additional two photons (Fig. 1).

The saturation of the t_{2g}-e_g transition and the competition between *2*PP and *3*PP is clearly evident in Fig. 6. The fluence dependent spectra are normalized at the work function edge, where the saturation effect is minimal and the *2*PP process does not appear to be enhanced by an intermediate state resonance. The Fermi edge for *2*PP is marked with a vertical line for reference. Even at lowest laser intensity there is some signal above the Fermi level edge due to the bandwidth of the laser, and thermal broadening of the Fermi distribution. The photoemission signal above the *2*PP Fermi edge can also have contributions from *3*PP and higher order processes.[69] At higher fluences, the relative intensity of the e_g peak decreases and the *3*PP intensity above the E_F limit increases. We confirmed that this effect is dependent on the peak and not the average power of the laser by varying its repetition rate and the pulse energy so as to keep the average power constant. This excludes the possibility that the *3*PP process involves a build up of carriers in the CB on the time scale between the laser excitation cycles or that the sample charging influences the spectra. Although under some circumstances the carrier lifetimes in TiO_2 can extend to the millisecond time scale,[70] the slow carrier recombination does not appear to affect the *m*PP signal from single crystal TiO_2 surface in vacuum at MHz repetition rates. It is possible that the carrier recombination in the absence of molecular electron or hole traps is sufficiently fast to remove CB carriers between each cycle of excitation, or that the upward band bending near the surface sweeps electrons into the bulk of the crystal where they are not detected.[71]

The photoelectron energy distributions in Fig. 6 reflect the nature of the *3*PP process. In metals under perturbative light-surface interaction, higher-order *m*PP processes usually involve above threshold photoemission, where absorption of an additional photon by electrons excited above E_{vac} creates a replica of the spectrum excited by the lower order process.[69] This clearly is not happening in TiO_2. The higher order *3*PP signal is initiated from the more deeply bound occupied states in the VB rather than replicating the *2*PP spectrum from the defects states. Therefore, one might expect the maximum photoelectron energy via the *3*PP process to correspond to emission from the VBM. From the spectra in Fig. 6 it is difficult to identify a clear VBM cutoff, which for the excitation of bulk rutile TiO_2 with three 3.5 eV photons should occur at 7.7 eV. Contrary to this expectation the observed spectrum extends beyond 8 eV. A possible explanation for this excess photoelectron energy is an upward surface band bending, which is ~0.4 eV for TiO_2 surfaces annealed in O_2 atmosphere.[71] Because the photoelectron escape depth is much less than the surface accumulation region, the *3*PP spectra can be strongly affected by the surface band bending. By contrast, the defect density distribution is pinned at the same Fermi level for the surface and in the bulk.

Under high-density excitation of a semiconductor surface it is possible to screen the surface fields, and thereby to flatten the surface bands. Such surface photovoltage effect has been claimed in *2*PP spectra of ZnO [38], though the same features can be explained by the formation of a surface exciton.[39] Flattening of the surface band bending should cause the CBM to shift with respect to E_F. In the present measurements, the CBM of $TiO_2(110)$ is not observed; therefore, the effect of surface photovoltage in the *m*PP spectra is difficult to identify among other nonlinear processes.

2. mPP photodynamics

In addition to the *m*PP spectra, we also measure ITR-*2*PC scans to gain information on the ultrafast electron photodynamics. Figure 7 shows an ITR-*2*PC scan obtained with identical 3.26 eV photon energy pump-probe pulses; the figure shows a cross section through the 3D data corresponding to *2*PP intensity *vs.* the final energy and delay time for the surface normal emission.[52] The interferogram in Fig. 7(b) is a line profile through the data for the final state energy of 6.2 eV, corresponding to the e_g resonance. The interferogram is indistinguishable from the pulse autocorrelation measured by *2*PP on the Mo sample holder. Its appearance, *i.e.*, the nearly 8:1 ratio of the fringe-to-background signal and duration of the interference, are consistent with a *2*PP process excited with <20 fs laser pulse. As in the previous measurements [25], we are not able to resolve the electron phase and population dynamics at 2-3 eV above the CBM of $TiO_2(110)$ upon excitation from the Ti-3*d* defect states.

When ITR-*2*PC is measured at 3.40 eV using a high laser fluence [Fig. 8(a)] the interferograms obtained from line profiles at different energies [Fig. 8(b) and (8c)] show evidence for more complex photodynamics than in Fig. 7. In Fig. 8(b), the interferogram at the 6.20 eV final state energy for the *2*PP excitation from the Ti-3*d* defect states through the e_g resonance shows clear evidence for the saturation of the optical transition in the clipping of the amplitude of the interference fringes at short delays and the small ratio of the fringe-to-background emission amplitude. By contrast, the *m*PP signal near the E_F edge (6.75 eV), *i.e.*, for the region where *3*PP from the VBM contributes to the photoemission signal, the line profile with a ratio of >8:1 is consistent with contribution from both *2*PP and *3*PP processes. This ratio becomes even larger for higher final state energies as the contribution from *3*PP increases relative to *2*PP. The saturation behavior is also observable in Fig. 8(d), which shows the amplitude of the *m*PP signal in Fig. 8(a) when the pump-probe delay is in-phase for the carrier wave of the excitation pulses. Near the zero delay, when the pump and probe excitation fields interact coherently, the peak in the *m*PP signal shifts to higher energy; this corresponds to the high intensity excitation in Fig. 6, where the t_{2g}-e_g transition is saturated and *3*PP process dominates. When the delay is increased beyond the range of pump and probe interferences, the signal maximum shifts to 6.2 eV, where it is expected from the low fluence measurement in Fig. 6. This is consistent with pump and probe pulses individually exciting *2*PP process from the Ti-3*d* defect states *via* the e_g intermediate state without a significant correlated contribution from transient changes in the electron and hole populations. If the carrier energy relaxation were to occur on the time scale comparable to the pump-probe delay, one would expect the pump pulse to deplete the defect states, and the probe emission to be diminished (*2*PP). Similarly, if the pump pulse would populate the CB of TiO_2, the delayed probe pulse induced emission would be enhanced (incoherent *3*PP).[72, 73] Such dynamics have been reported in two-color *2*PP measurements on ZnO, where high photon energy UV probe pulses excite single photon emission from near the E_F,[38, 39] instead of the one-color experiments performed here, where the hot carrier distributions can only be interrogated by two-photon absorption. The fact that the population relaxation is not evident in ITR-*2*PC measurements is consistent with the *2*PP and *3*PP processes reported herein being dominated by the coherent interactions involving the intermediate and possibly final state resonances. It appears that incoherent, hot electron mediated pathways, such as described by the dark green arrows in Fig. 1, make negligible contributions. It is also possible that carrier relaxation by e-p and e-e scattering in TiO_2 is much faster than our pulse duration, which would be consistent with the calculated hot electron lifetimes.[36, 37] The hot-carrier dynamics in TiO_2 are likely to be more easily resolved in two-color experiments near the CBM, as has been done for ZnO.[38, 39]

IV. Conclusion

Multi-photon photoemission is carried out on a $TiO_2(110)$ surface using 2.95-4.59 eV photon energy light with <20 fs pulse duration. For excitation with 3.2 eV and higher photon energy we find a distinct pair of nearly degenerate unoccupied bulk states of TiO_2 at 2.73±0.05 and 2.85±0.05 eV above the Fermi level. These states are excited from the O atom vacancy defect states and are consistent with transitions between the Ti-3*d* band of t_{2g}- and e_g-symmetry, which are split by the crystal field. Polarization and crystal orientation dependent measurements of the t_{2g}-e_g transition reflect the anisotropy of the TiO_2 rutile crystalline lattice. In particular, the t_{2g}-e_g transition from the defect states dominates the *2*PP spectra when the electric field of the excitation laser points in the $[1\bar{1}0]$ crystalline direction; this implicates transitions from defect states with the same symmetry as the CBM+1 band. The spectroscopic assignment of this resonance is supported by DFT calculations, which confirm the anisotropic nature of the excitation process. Time resolved measurements are performed to probe the e_g state lifetime, as well as those of the hot carriers near the Fermi level. In both cases, the lifetimes appear to be <20 fs, though the preference for coherent pathways in the *m*PP measurements may make contributions of hot carrier populations difficult to observe.[72, 73] The ultrafast decay of the e_g state most likely makes it inactive in TiO_2 photocatalysis, though it may be useful for optical probing of the charge carrier dynamics within the VB and CB of TiO_2. The lack of observable electron relaxation processes even from the e_g resonance is consistent with the previous measurements on clean TiO_2 surfaces,[25] and confirm that the long electron lifetimes for catechol covered TiO_2 surface[31] do not represent intrinsic hot electron dynamics of TiO_2. Finally, the saturation effect at high laser fluences leads to a shift and broadening of the e_g peak due to the depletion of the defect carrier density. 3D time-resolved photoemission measurements show evidence for the competition between the *2*PP and *3*PP processes at the onset of the direct band gap excitation of TiO_2. Future work will focus on the investigation of the hot carrier dynamics using two-color *2*PP measurements.

Acknowledgements. We acknowledge funding from NSF Grant No. CHE-1213189, and computational time from Environmental Molecular Sciences Laboratory at the PNNL, a user facility sponsored by the DOE Office of Biological and Environmental Research.

V. References

1. A. Fujishima and K. Honda, Nature **238**, 37 (1972).
2. M. Gratzel, Nature **414**, 338 (2001).
3. M. R. Hoffmann, S. T. Martin, W. Choi, and D. W. Bahnemann, Chem. Rev. **95**, 69 (1995).
4. T. L. Thompson and J. T. Yates, Jr., Chem. Rev. **106**, 4428 (2006).
5. A. Fujishima, X. Zhang, and D. A. Tryk, Surf. Sci. Rep. **63**, 515 (2008).
6. C. L. Pang, R. Lindsay, and G. Thornton, Chem. Soc. Rev. **37**, 2328 (2008).
7. M. A. Henderson, Surf. Sci. Rep. **66**, 185 (2011).
8. O. V. Prezhdo, W. R. Duncan, and V. V. Prezhdo, Prog. Surf. Sci. **84**, 30 (2009).
9. D. M. Adams, et al., J. Phys. Chem. B **107**, 6668 (2003).
10. J. i. Kanasaki, H. Tanimura, and K. Tanimura, Phys. Rev. Lett. **113**, 237401 (2014).
11. J. B. Asbury, E. Hao, Y. Wang, H. N. Ghosh, and T. Lian, J. Phys. Chem. B **105**, 4545 (2001).
12. T. Yoshihara, R. Katoh, A. Furube, Y. Tamaki, M. Murai, K. Hara, S. Murata, H. Arakawa, and M. Tachiya, J. Phys. Chem. B **108**, 3817 (2004).
13. E. Hendry, F. Wang, J. Shan, T. F. Heinz, and M. Bonn, Phys. Rev. B **69**, 081101 (2004).
14. Y. Tamaki, A. Furube, M. Murai, K. Hara, R. Katoh, and M. Tachiya, J. Am. Chem. Soc. **128**, 416 (2006).
15. Y. Tamaki, A. Furube, M. Murai, K. Hara, R. Katoh, and M. Tachiya, Phys. Chem. Chem. Phys. **9**, 1453 (2007).
16. F. J. Knorr, C. C. Mercado, and J. L. McHale, J. Phys. Chem. C **112**, 12786 (2008).
17. Y. Tamaki, K. Hara, R. Katoh, M. Tachiya, and A. Furube, J. Phys. Chem. C **113**, 11741 (2009).
18. T. Nomoto, A. Sasahara, and H. Onishi, J. Chem. Phys. **131**, 084703 (2009).
19. R. Katoh, M. Murai, and A. Furube, Chem. Phys. Lett. **500**, 309 (2010).
20. K. Ishioka and H. Petek, Phys. Rev. B **86**, 205201 (2012).
21. E. M. Bothschafter, A. Paarmann, E. S. Zijlstra, N. Karpowicz, M. E. Garcia, R. Kienberger, and R. Ernstorfer, Phys. Rev. Lett. **110**, 067402 (2013).
22. H. Petek and S. Ogawa, Prog. Surf. Sci. **56**, 239 (1997).
23. M. Weinelt, J. Phys.: Condens. Matter **14**, R1099 (2002).
24. K. Onda, B. Li, and H. Petek, Phys. Rev. B **70**, 045415 (2004).
25. K. Onda, B. Li, J. Zhao, K. D. Jordan, J. Yang, and H. Petek, Science **308**, 1154 (2005).
26. K. Onda, B. Li, J. Zhao, and H. Petek, Surf. Sci. **593**, 32 (2005).
27. B. Li, J. Zhao, K. Onda, K. D. Jordan, J. Yang, and H. Petek, Science **311**, 1436 (2006).
28. J. Zhao, B. Li, K. Onda, M. Feng, and H. Petek, Chem. Rev. **106**, 4402 (2006).
29. H. Petek and J. Zhao, Chem. Rev. **110**, 7082 (2010).
30. D. Ino, K. Watanabe, N. Takagi, and Y. Matsumoto, J. Phys. Chem. B **109**, 18018 (2005).
31. L. Gundlach, R. Ernstorfer, and F. Willig, Phys. Rev. B **74**, 035324 (2006).
32. L. Gundlach, R. Ernstorfer, and F. Willig, Prog. Surf. Sci. **82**, 355 (2007).
33. L. Gundlach, J. Szarko, L. D. Socaciu-Siebert, A. Neubauer, R. Ernstorfer, and F. Willig, Phys. Rev. B **75**, 125320 (2007).
34. T. Minato, et al., J. Chem. Phys. **130**, 124502 (2009).
35. V. E. Henrich, Prog. Surf. Sci. **9**, 143 (1979).
36. V. P. Zhukov and E. V. Chulkov, J. Phys.: Condens. Matter **22**, 435802 (2010).
37. K. Ali, Physica Scripta **90**, 025804 (2015).
38. W. A. Tisdale, M. Muntwiler, D. J. Norris, E. S. Aydil, and X. Y. Zhu, J. Phys. Chem. C **112**, 14682 (2008).
39. J. C. Deinert, D. Wegkamp, M. Meyer, C. Richter, M. Wolf, and J. Stähler, Phys. Rev. Lett. **113**, 057602 (2014).
40. J. Zhao, B. Li, K. D. Jordan, J. Yang, and H. Petek, Phys. Rev. B **73**, 195309 (2006).
41. A. Migani, D. J. Mowbray, A. Iacomino, J. Zhao, H. Petek, and A. Rubio, J. Am. Chem. Soc. **135**, 11429 (2013).

42. A. Migani, D. J. Mowbray, J. Zhao, H. Petek, and A. Rubio, J. Chem. Theo. Comput. **10**, 2103 (2014).
43. A. Migani, D. J. Mowbray, J. Zhao, and H. Petek, J. Chem. Theo. Comput. **11**, 239 (2015).
44. H. Petek, J. Chem. Phys. **137**, 091704 (2012).
45. R. Huber, J.-E. Moser, M. Grätzel, and J. Wachtveitl, J. Phys. Chem. B **106**, 6494 (2002).
46. V. Eyert, Annalen der Physik **11**, 650 (2002).
47. N. B. Aetukuri, et al., Nat Phys **9**, 661 (2013).
48. D. Wegkamp, et al., Phys. Rev. Lett. **113**, 216401 (2014).
49. C. Homann, C. Schriever, P. Baum, and E. Riedle, Opt. Express **16**, 5746 (2008).
50. C. Schriever, S. Lochbrunner, P. Krok, and E. Riedle, Opt. Lett. **33**, 192 (2008).
51. S. Ogawa, H. Nagano, H. Petek, and A. P. Heberle, Phys. Rev. Lett. **78**, 1339 (1997).
52. X. Cui, C. Wang, A. Argondizzo, S. Garrett-Roe, B. Gumhalter, and H. Petek, Nat Phys **10**, 505 (2014).
53. D. A. Panayotov, S. P. Burrows, and J. R. Morris, J. Phys. Chem. C **116**, 4535 (2012).
54. L. Chiodo, J. M. García-Lastra, A. Iacomino, S. Ossicini, J. Zhao, H. Petek, and A. Rubio, Phys. Rev. B **82**, 045207 (2010).
55. K. Vos, J. Phys. Chem. **10**, 3917 (1977).
56. M. A. Henderson, W. S. Epling, C. H. F. Peden, and C. L. Perkins, J. Phys. Chem. B **107**, 534 (2003).
57. S. Moser, et al., Phys. Rev. Lett. **110**, 196403 (2013).
58. K. F. Wall and A. Sanchez, The Lincoln Laboratory Journal **3**, 447 (1990).
59. W. Kang and M. S. Hybertsen, Phys. Rev. B **82**, 085203 (2010).
60. M. S. Hybertsen and S. G. Louie, Phys. Rev. B **34**, 5390 (1986).
61. B. A. Ruzicka, L. K. Werake, H. Samassekou, and H. Zhao, Appl. Phys. Lett. **97**, 262119 (2010).
62. J. P. Perdew, K. Burke, and M. Ernzerhof, Phys. Rev. Lett. **77**, 3865 (1996).
63. See Supplemental Material at for the claculated transition densities from the CBM of TiO_2.
64. V. M. Khomenko, K. Langer, H. Rager, and A. Fett, Phys. Chem. Miner. **25**, 338 (1998).
65. D. W. Fischer, Phys. Rev. B **5**, 4219 (1972).
66. L. A. Grunes, Phys. Rev. B **27**, 2111 (1983).
67. A. K. See, M. Thayer, and R. A. Bartynski, Phys. Rev. B **47**, 13722 (1993).
68. L. Fleming, C. C. Fulton, G. Lucovsky, J. E. Rowe, M. D. Ulrich, and J. Lüning, J. Appl. Phys. **102**, 033707 (2007).
69. F. Bisio, M. Nývlt, J. Franta, H. Petek, and J. Kirschner, Phys. Rev. Lett. **96**, 087601 (2006).
70. A. Yamakata, T.-a. Ishibashi, and H. Onishi, J. Mol. Catal. A **199**, 85 (2003).
71. Z. Zhang and J. T. Yates, Jr., Chem. Rev. **112**, 5520 (2012).
72. M. J. Weida, S. Ogawa, H. Nagano, and H. Petek, J. Opt. Soc. Am. B **17**, 1443 (2000).
73. M. J. Weida, S. Ogawa, H. Nagano, and H. Petek, Appl. Phys. A **71**, 553 (2000).

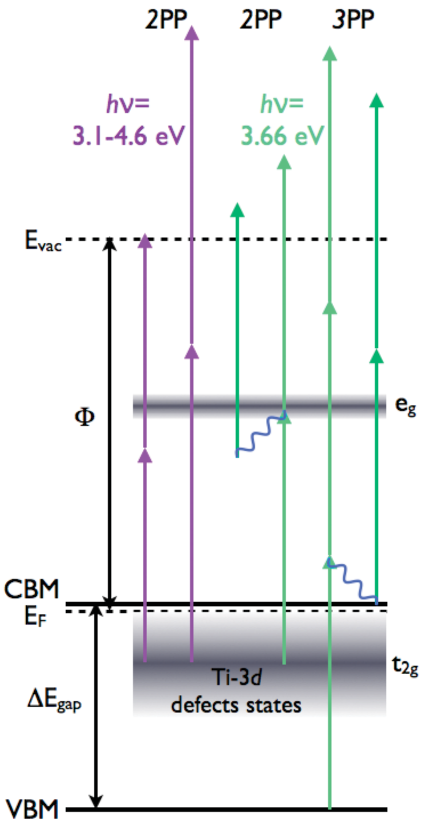

FIG. 1 (Color online)- *m*PP excitation diagram for the clean, reduced rutile $TiO_2(110)$ surface. With *hv*=3.1-4.6 eV (purple arrows), *2*PP processes are excited from the Ti-3*d* defect states. Resonant *2*PP excitation from the t_{2g} symmetry defect states to the nearly degenerate e_g bands occurs with *hv*=3.66 eV. Under high density excitation there is concomitant *3*PP excitation from the VBM. These processes can be coherent (light green) or sequential (dark green), where hot electron relaxation (squiggly blue lines) can occur within the CB. Black arrows designate the work function Φ and the band gap, ΔE_{gap}.

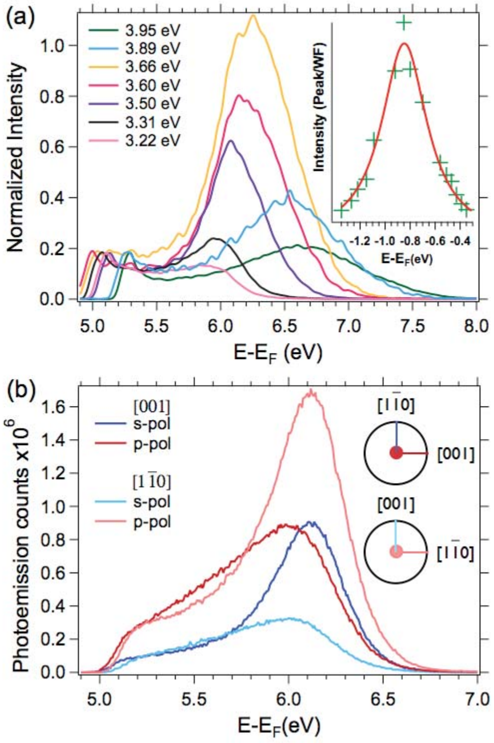

FIG. 2 (Color online)-**(a)** Excitation dependent *2*PP spectra of clean $TiO_2(110)$ surface showing the emergence of a peak for *hv*≥3.2 eV (380 nm). The spectra are normalized to the work function edge. Inset: Distribution of the peak *2*PP intensity relative to the work function intensity, which is attributed to the defect density of states below the Fermi level. **(b)** 2PP spectra excited with *p*- and *s*-polarized light for 3.26 eV photon energy with the [001] or $[1\bar{1}0]$ crystalline axes oriented in the optical plane. The diagrams on the right indicate the crystal orientation with respect to the optical plane (horizontal), while the colored lines and circles indicate the in-plane and surface normal components of the excitation field $\vec{E}$.

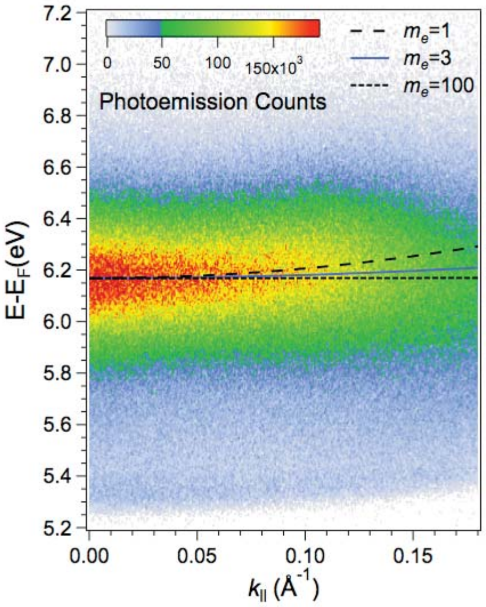

FIG. 3 (Color online)-Energy *vs.* momentum plot of *2*PP intensity with 3.60 eV excitation showing the weak dispersion of the e_g state. Due to a limited momentum range of the measurement and the broad width of the resonance the effective mass of m_e=3 has a high uncertainty bracketed by the dashed lines for m_e=1 and 100.

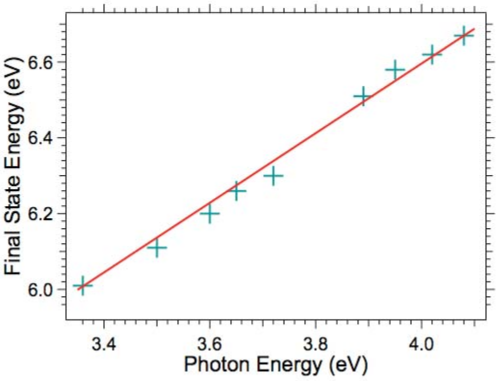

FIG. 4 (Color online)- Final State Energy *vs*. Photon Energy for the e_g peak. The slope of approximately one confirms the e_g band to be an intermediate state in the *2*PP process.

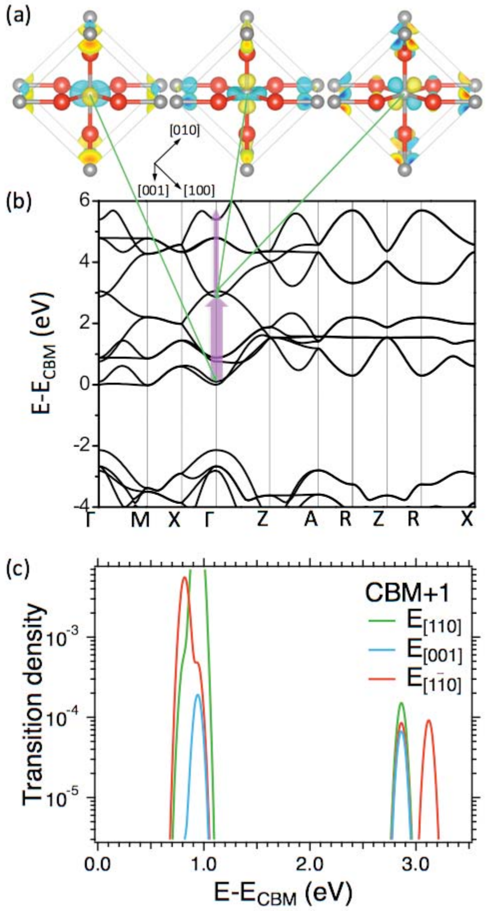

FIG. 5 (Color online)- **(a)** The Ti-3*d* orbitals involved in the optical transitions that contribute to the *2*PP spectra at the Γ point. From left to right the orbitals correspond to the CBM+1, 2.85, and 3.11 eV bands. **(b)** The band structure of TiO_2 rutile from DFT calculations. The fat arrow indicates the t_{2g}-e_g resonance at the Γ point. The thin arrow represents photoemission from the transiently excited e_g state. **(c)** The calculated transition density for *d*-*d* transitions from the CBM+1 excited by for $\vec{E}$ pointing in the [001], $[1\,\bar{1}0]$, and [110] directions. The energy origin is the CBM.

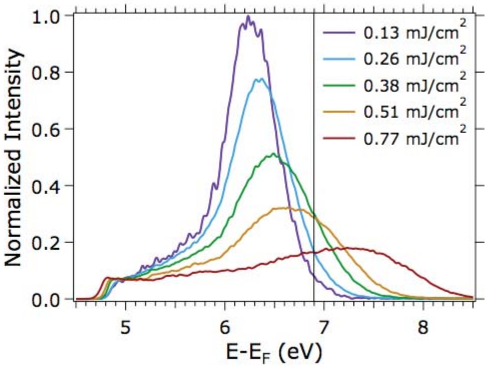

FIG. 6 (Color online)- *m*PP spectra for various laser fluences for excitation at 3.50 eV (354 nm) showing the saturation of the t_{2g}-e_g transition and the onset of *3*PP above the *2*PP Fermi level edge (black line). The spectra are normalized at the work function edge.

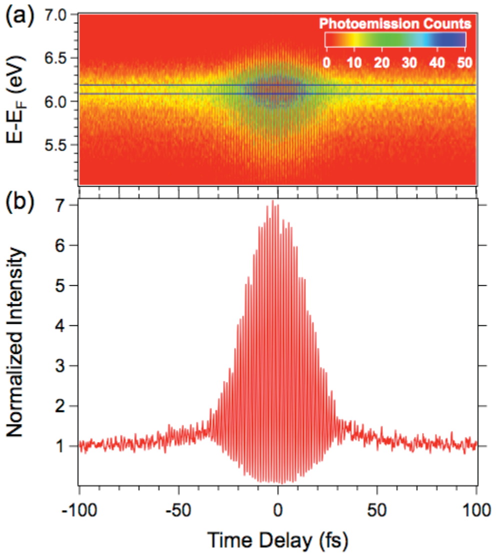

FIG. 7 (Color online)- **(a)** Interferometric two-pulse correlation measurement for ±100 fs delay taken with *hv*=3.27 eV for the TiO_2 sample. **(b)** Line profile of the data for the energy range shown by the black lines in (a). The interferogram corresponds to a pulse duration of ~20 fs; its nearly 8 to 1 intensity ratio is expected for a two-photon process.

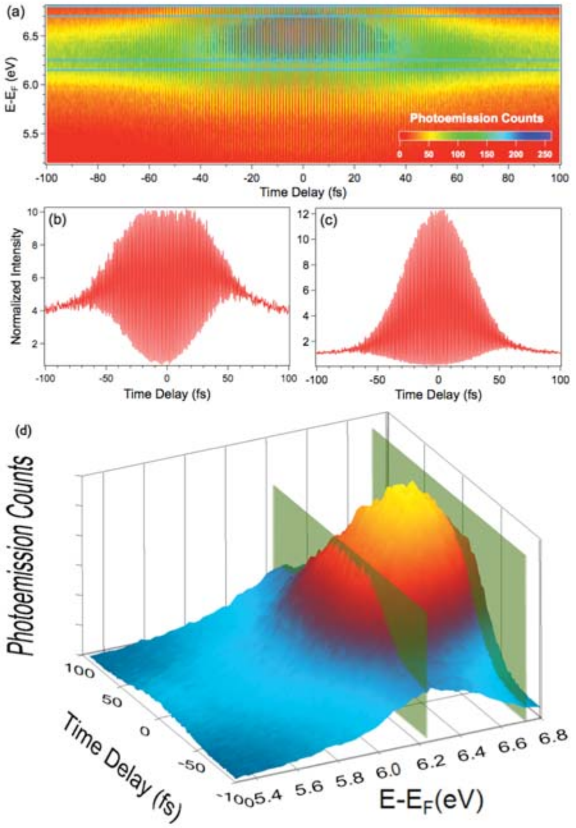

FIG. 8 (Color online)- **(a)** Interferometric two-pulse correlation measurement taken with *hv*=3.40 eV for the TiO_2 sample under saturation fluence. **(b)** line profile taken at 6.20 eV, corresponding to the photoelectron energy where the e_g peak energy would be observed at low laser fluence or long delay times (*e.g.*, ±100 fs). **(c)** line profile taken at 6.75 eV, corresponding to the peak in the photoelectron signal under saturation fluence at 0 fs delay. The peak-to-background ratios show evidence of the *2*PP saturation (b) and contribution from *3*PP (c) at high laser fluences. (b) and (c) are plotted on the same relative intensity scale. **(d)** A quasi-3D plot of the in-phase contribution of the ITR-*2*PC signal in (a) showing the photoemission energy distributions at different delay times with the energies for the cross sections in (b) and (c) designated by the intersecting planes.